Advances in Aerodynamics

RESEARCH Open Access

Open-jet facility for bio-inspired micro-air-vehicle flight experiment at low speed and high turbulence intensity

Zhifeng Liu[1] and Yue Yang[1,2*]

*Correspondence:
yyg@pku.edu.cn

[1] State Key Laboratory for Turbulence and Complex Systems, College of Engineering, Peking University, Beijing 100871, China
[2] HEDPS-CAPT, Peking University, Beijing 100871, China

Abstract

Bio-inspired micro-air-vehicles (MAVs) usually operate in the atmospheric boundary layer at a low Reynolds number and complex wind conditions including large-scale turbulence, strong shear, and gusts. We develop an open jet facility (OJF) to meet the requirements of MAV flight experiments at very low speed and high turbulence intensity. Powered by a stage-driven fan, the OJF is capable of generating wind speeds covering 0.1 – 16.8 m/s, with a velocity ratio of 100:1. The contraction section of the OJF is designed using an adjoint-driven optimization method, resulting in a contraction ratio of 3:1 and a length-to-diameter ratio of 0.75. A modularized design of the jet nozzle can produce laminar or high-turbulence wind conditions. Flow field calibration results demonstrate that the OJF is capable of producing a high-quality baseline flow with steady airspeed as low as 0.1 m/s, uniform region around 80% of the cross-sectional test area, and turbulence intensity around 0.5%. Equipped with an optimized active grid (AG), the OJF can reproduce controllable, fully-developed turbulent wind conditions with the turbulence intensity up to 24%, energy spectrum satisfying the five-thirds power law, and the uniform region close to 70% of the cross-sectional area of the test section. The turbulence intensity, integral length scale, Kolmogorov length scale, and mean energy dissipation rate of the generated flow can be adjusted by varying the area of the triangular through-hole in the wings of the AG.

Keywords: Open-jet facility, Active grid, MAV flight, High turbulence intensity

1 Introduction

In recent years, micro-air-vehicles (MAVs) employed the flight characteristics of natural flyers, such as birds, bats, and insects at low Reynolds numbers $Re = 10^2 - 10^4$, with growing interests for their small size, low weight, and good stealthiness [1–3]. With excellent agility and flight performance, small natural flyers can navigate in densely cluttered environments and fly under unsteady wind conditions with strong turbulence, wind shear, and gusts [4–7]. Most challenging issues of bio-inspired vehicles and natural flyers include the unsteady flow phenomenon and aerodynamic performance of complex flapping wing motions in low-*Re* and highly unsteady wind environments [1, 8, 9].

Previous studies of experimental diagnostics, computational fluid dynamics (CFD), and theoretical modeling showed that the flyers employ several unsteady aerodynamic mechanisms, including clap and fling [10], delayed stall [11], added-mass effect [12, 13], and paddling [14–19], to gain enough lift to counteract their weight, or thrust to exceed the drag. However, these mechanisms are far from being fully understood due to their complex flight parameters and challenging flight control strategies in highly unsteady flows with turbulence and gusts. Since these problems are still hard to be fully solved by state-of-the-art CFD techniques, it is necessary to obtain sufficient experiment data of the unsteady aerodynamics in a wind tunnel generating low-*Re* and highly unsteady flow conditions.

A wind tunnel is a pipe-like facility generating controllable airflow extensively used in the laboratories [20, 21], but there is a lack of specially designed wind tunnels for insects and bio-inspired MAV flight experiments at a wide range of $Re = 10^2 - 10^4$. Such a wind tunnel requires the ability to generate a controllable flow with the airspeed range covering the flight speed of typical insects (e.g., mosquito: $1.6 - 2.4$ km/h [22], honeybee: 27 km/h [23], and dragonfly: 54 km/h [24]), and create the unsteady flow environment with large-scale turbulence, wind shear, and gusts [4–7, 25]. The design and construction of the wind tunnel also prefers a sizeable test area, low cost, and ease of use.

A general-purpose low-speed wind tunnel usually generates a uniform flow with a low turbulence intensity, an airspeed of $5 - 100$ m/s, and a maximum-to-minimum velocity ratio ≈ 10. Several studies obtained the flow with an ultra-low airspeed less than 1 m/s in the wind tunnel. Plate and Cermak [26] used a variable pitch propeller driven by a stabilized DC motor with $230 - 1450$ rpm to control the airspeed of $1 - 30$ m/s, but this sophisticated technique is costly for the implementation and maintenance of the wind tunnel. Other methods for lowering the airspeed include using the auxiliary exhaust duct, valves, and low-speed driven motors. Terao et al. [27] used shut valves to control the flow rate of a suction-type wind tunnel, achieving an operating airspeed of $0.045 - 1.4$ m/s. Sun and Zhu [28] designed an open-jet wind tunnel using micro-regulating exhaust holes after the power section, achieving an airspeed of $1 - 13$ m/s. Leith et al. [29] designed a wind tunnel driven by a micro-stepping motor, generating a working airspeed of $0.03 - 3$ m/s. Pezzotti et al. [30] built a suction-type wind tunnel powered by a blower, generating a low-speed range of $0.2 - 1.25$ m/s for anemometer calibration. These approaches are suitable for mini wind tunnels for anemometer calibration but hard to be extended to large ones for MAV flight experiments.

Generating highly unsteady wind conditions is challenging in the laboratory. Early methods employed grids and stakes in the wind tunnel to generate turbulent flows [31–34]. Later, active systems were used, e.g., the jet grid/array [35, 36], active grid (AG) [37], multiple controlled fans [38–43]. In particular, the "Makita-style" AG showed advantages in terms of high turbulence intensity, real-time adjustable parameters, and easy integration to the existing wind tunnel. It is multifunctional to produce various unsteady flows [44–49]. Some wind tunnels [50–52] integrated the Makita-style AG in the open-jet test section to conduct flight experiments of flying animals and MAVs at $Re = 10^4 - 10^5$.

The experimental models placed in the open-jet region at the AG downstream lead to conflicting requirements. When the turbulent jet fully develops further downstream,

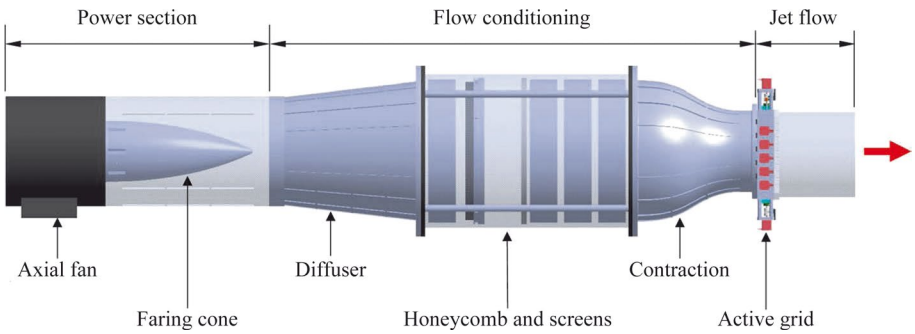

Fig. 1 Schematic of the OJF

the open jet flow diffuses with a diminishing uniform region. Therefore, it is critical to properly install and optimize the AG in the open-jet test section to produce a sizeable uniform test area (more than 70% of test section's cross-sectional width/height) with controllable turbulence intensity (10% − 20%).

The present study designs and constructs a blower-type open-jet facility (OJF) for bio-inspired MAV flight experiments at low speed and high turbulence intensity. It is also featured by the low construction cost, small footprint area, and good extensibility. The OJF design is described in Section 2. The OJF consists of a stage-driven fan, an optimized flow conditioning section, and a modular, interchangeable nozzle with the AG. It can generate steady laminar jet flows or controllable, fully developed turbulent jet flows. The flow quality of a sub-scale prototype wind tunnel is assessed in Section 3. Conclusions are drawn in Section 4.

2 Design of the open-jet facility

As sketched in Fig. 1, the OJF consists of three parts – the power section, the flow conditioning section, and the modularized jet flow generation system. An airflow is first driven by an axial fan. Then the flow conditioning section re-laminarizes the flow. Finally, the modularized system can generate different wind conditions, including laminar and turbulent jets.

2.1 Drive system

A powerful, high-precision drive system is essential for generating an air flow at a wide range of $Re = 10^2 - 10^4$ in the test section of a wind tunnel. As shown in Fig. 2a, it consists of an eight-blade fan, a nine-vane anti-twisting deflector, a faring cone, a 315 W brushless DC electric motor, and a step motor. The design methods for the fan and stator can be found in Refs. [53, 54]. The DC motor, with its rotor and stator embedded in the fan and deflector, respectively, powers the fan running at speed from 1000 to 3000 rpm. To obtain a lower, stable speed from 10 to 1000 rpm, a 57-step motor (around 60 W) with a long axis links the rotor through shaft coupling. Additionally, a streamline faring cone improves airflow performance at fan downstream. As marked by "power section" in Fig. 1, the drive system, housed in a 315 mm diameter, 815 mm long circular duct, generates an axial airflow.

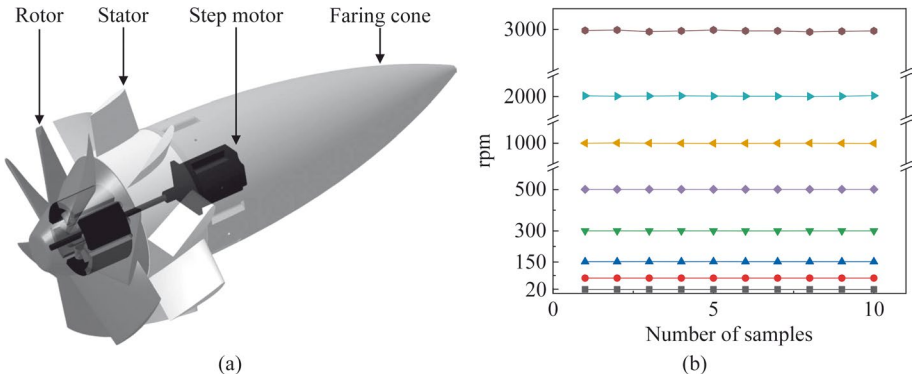

Fig. 2 **a** Schematic of the drive system. **b** Steadiness of the fan speed

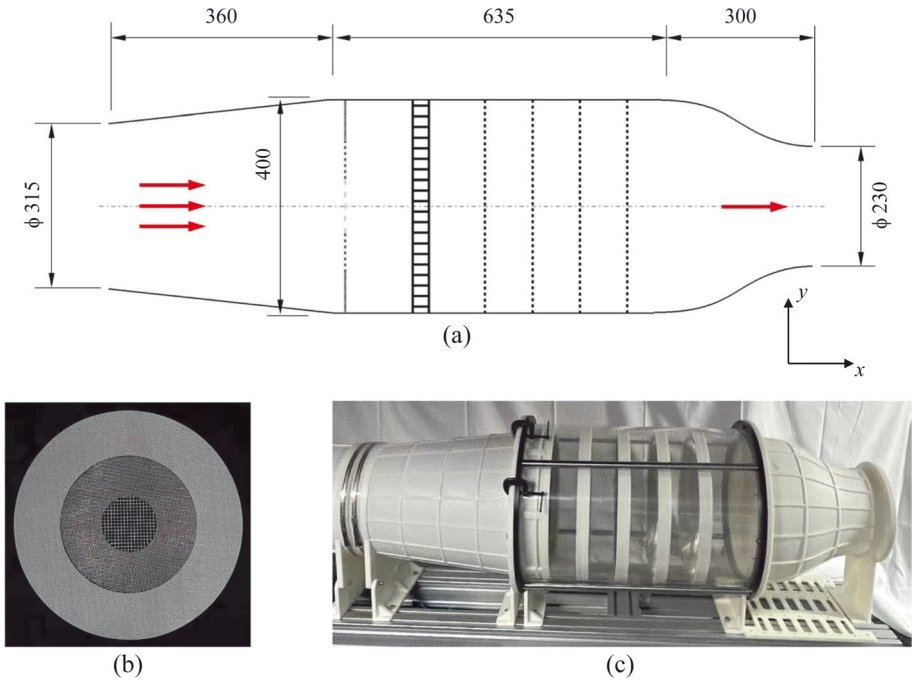

Fig. 3 **a** Schematic of the flow conditioning section (all dimensions in mm). **b** Variable-density damping screen. **c** Flow conditioning section of the sub-scale prototype OJF

Figure 2b demonstrates the steadiness of the fan rotating at various speeds, measured with a Testo 470 handheld tachometer. The horizontal axis shows the number of sample points at one-minute intervals, and the vertical axis shows the speed of rotation. The stage-driven scheme successfully drives the fan operating at a wide speed range from 19.1 to 3000 rpm with a relative standard deviation (RSD) less than 0.2%, and its cost is much lower than that of large servo motors or DC motors. Moreover, it is straightforward to scale up the power section to larger wind tunnel sizes.

2.2 Flow conditioning

In Fig. 3, from left to right, the flow conditioning section includes a diffuser, a variable-density damping screen, a honeycomb, and homogeneous damping screens to straighten

and laminarize the flow. The diffuser, with a divergence angle of 6.73°, converts kinetic energy into pressure energy. A variable-density damping screen is installed downstream to pre-rectify the velocity deficit in the central region of the axial fan wake, as shown in Fig. 3b. The variable-density damping screen is made of three circular mesh layers with different mesh counts welded together – the outer mesh (outer diameter 400 mm, inner diameter 250 mm, 24 mesh counts, and wire diameter around 0.2 mm), middle mesh (outer diameter 250 mm, inner diameter 100 mm, 18 mesh counts, and wire diameter around 0.25 mm), and inner mesh (diameter 100 mm, 10 mesh counts, wire diameter around 0.35 mm). A honeycomb (hexagonal cell of width 3.2 mm, wall thickness 0.1 mm, and length-to-diameter ratio of 10) and four homogeneity damping screens (with nominal apertures of 2×2 mm^2 and open areas of 72%) are employed to straighten the flow and suppress turbulence.

At the last screen downstream, a contraction is applied to accelerate the flow and improve the flow quality, i.e., the uniformity and steadiness, at the test section. Many factors should be considered in contraction design, including the contraction ratio, length, wall shape, and manufacturing method, and they determine the flow quality, size of the test section, and cost. Typical design methods include potential flow theory, CFD, and simulation-driven optimization methods [55–58]. These methods typically adopted a uniform velocity inlet boundary, combined with contraction ratios of 6 to 10:1 and length of $0.75 - 2D_i$ to improve the flow quality in the test section, where D_i denotes the contraction inlet diameter. The present OJF for MAV flight experiments in an atmospheric boundary layer aims to reproduce unsteady wind conditions in a relatively sizeable experimental area, so we adopted a very small contraction ratio of 3:1, and used an adjoint-driven method [59, 60] to optimize the contraction shape.

The CFD and adjoint simulations were conducted using ANSYS Fluent 19.0. As shown in Fig. 4a, the computational domain is an axisymmetric plane for the contraction. It consists of an inlet, a leading portion with the length of $0.075D$, a contraction section, a straight nozzle with the length of $0.5D$, and an outlet. Here, $D = 230$ mm was set for the diameter of the contraction exit. A measured airspeed profile at the fan speed 1700 rpm (blue solid line in Fig. 4c) was set as the inlet boundary condition, with a turbulence intensity of 2%. The pressure outlet boundary condition was applied, and the non-slip boundary conditions were applied for walls of the leading portion, contraction, and straight nozzle. The flow was solved in a steady state with spatially resolved boundary layers at $y^+ < 1$, where y^+ denotes the wall unit [61].

The optimization aims to minimize the variance of the time-averaged axial velocity and the magnitude of the time-averaged radial velocity. Thus, the adjoint observable is defined as

$$J = \frac{\sum_f A_f \left(U_f - \overline{U}_f\right)^2}{\sum_f A_f U_{o,\text{in}}^2} + \beta \frac{\sum_f A_f |V_f|}{\sum_f A_f U_{o,\text{in}}}, \tag{1}$$

where the subscript f denotes the cell facet, A_f is the facet area, U_f is the locally time-averaged axial velocity on the facet f, V_f is the locally time-averaged radial velocity on f, $\overline{U}_f$ is the averaged U_f over the region $(x/D, y/D) \in [0.25, 0.5] \times [0, 0.475]$, $U_{o,\text{in}}$ is the axial velocity at the inlet center, and $\beta = 10$ is a weight.

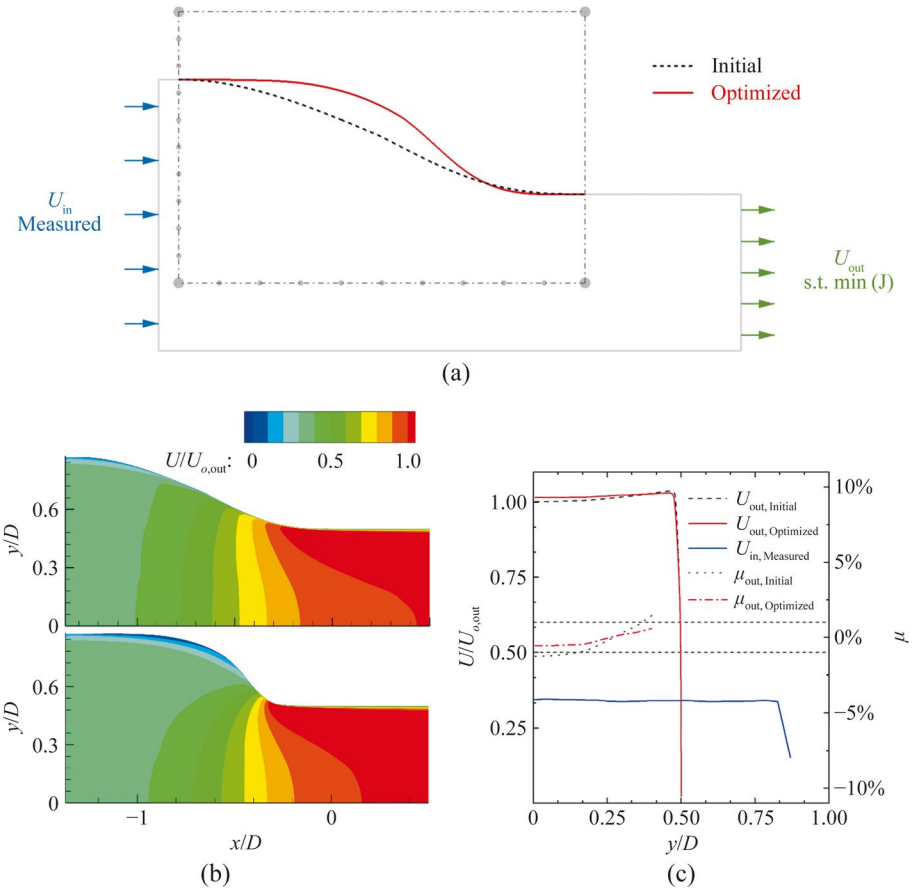

Fig. 4 **a** Schematic for the optimization of the contraction wall shape in the *x*–*y* symmetry plane, with the control volume (grey dashed line) and 11 control points (dots) in *x*- and *y*-directions. **b** Velocity contours of the initial (upper) and optimized (lower) contractions in the symmetry plane, where $U_{o,out}$ is the axial velocity at the outlet center ($(x/D, y/D, z/D) = (0.5, 0, 0)$) of the initial contraction. **c** Axial velocity profiles at the outlet ($x/D = 0.5$). The velocity profiles at the outlet of the initial contraction and the optimized contraction are labeled as $U_{\text{out, Initial}}$ and $U_{\text{out, Optimized}}$, respectively. The measured velocity profile at the inlet of the contraction is labeled as $U_{\text{in, Measured}}$. The flow uniformity in region $S = \{(x/D, z/D) = (0.5, 0), y/D \in [0, 0.4]\}$ is represented by $\mu_{\text{out, Initial}}$ for the initial contraction and $\mu_{\text{out, Optimized}}$ for the optimized contraction

In Fig. 4a, the shape to be optimized is enclosed by the dash-dotted lines, with 11 control points in both *x*- and *y*-directions. The black dashed line represents the contraction shape designed by matching 3rd- and 5th-order curves [55, 62], and the red solid line represents the optimized shape calculated with the adjoint solver. Figure 4b shows velocity contours in the contraction before and after optimization, where the velocity is calculated by the 2D Reynolds-averaged Navier–Stokes simulation with the SST $k - \omega$ model and axisymmetric swirl correction [63].

Figure 4c displays the axial velocity profiles at the outlet resulting from the initial contractions and the optimized contractions. The flow uniformity of the velocity profile over a region S is defined by

$$\mu = \frac{U - \overline{U}}{\overline{U}}, \tag{2}$$

where U denotes the time-averaged axial velocity, and $\overline{U}$ denotes the averaged U over the region S. The results demonstrate that the optimized contraction produces a more uniformly distributed velocity within a cross-sectional plane $S = \{(x/D, z/D) = (0.5, 0), y/D \in [0, 0.4]\}$.

Although the turbulence intensity and non-uniformity under the current 3:1 contraction ratio may be slightly higher than those under larger contraction ratios of 6 to 10:1 (with turbulence intensity less than 0.2% and non-uniformity less than 0.5%) in typical aeronautical wind tunnels, it fulfills the requirements for flight experiments involving MAVs operating within the atmospheric boundary layer. Furthermore, with equivalent footprint areas and construction costs, the effective cross-sectional area of the test section with the current 3:1 contraction ratio is one to two times larger than that of conventional designs with contraction ratios of 6 to 10:1.

2.3 Jet generation

The modularized jet generation section can be tested in two configurations. First, the baseline laminar-jet (LJ) configuration generates a uniform flow with low turbulence intensity. Here, $Tu = \sqrt{\sum_{i=1}^{N} u^2/N}/U$ is calculated over N samples of measured instantaneous streamwise velocity u.

In the implementation, a straight round nozzle with the diameter $1D$ and length $0.5D$ is connected to the contraction outlet with the diameter to improve flow uniformity [64].

Second, the turbulent-jet (TJ) configuration consisting of an AG and an extension nozzle is equipped at the outlet of the straight nozzle. This configuration produces a turbulent flow for testing insect/MAV flight in an atmospheric boundary layer. The grid consists of 10 rows and 10 columns of agitator wings, which are actuated independently by 20-step motors. In order to generate turbulent jets with controllable Tu, an improved AG consisting of agitator wings is used. Each wing has an isosceles right-triangular hole. By varying the hole size characterized by the porosity ratio R_p (defined in Fig. 5c), the blockage is adjusted to vary Tu and integral length scale L. An extension nozzle with the diameter $1D$ and length $1D$ connected to the contraction exit is installed at the AG downstream to ensure that the jet reaches the fully-developed turbulent state in the test section.

3 Assessment of flow quality

To assess the flow quality of the OJF in the LJ/TJ configuration, several experiments were conducted to evaluate the flow steadiness, uniformity, and turbulence intensity. Experimental setups are sketched in Fig. 6. A TSI IFA-300 constant temperature hot-wire anemometry (HWA) system, incorporating a single hot-film probe (model 1210-20), was used to acquire the airspeed and turbulence intensity. The probe was calibrated by the TSI model 1128B calibrator, with a relative calibration error less than 2%. An automatic XY positioning stage controlled the movement of the hot film probe to the measurement points. In the experiment, the room temperature was kept at 26 ± 0.5 °C. A Testo 622 thermo hygrometer and barometer measured the ambient absolute pressure and air temperature. In addition, measurement uncertainties, associated with bias and random

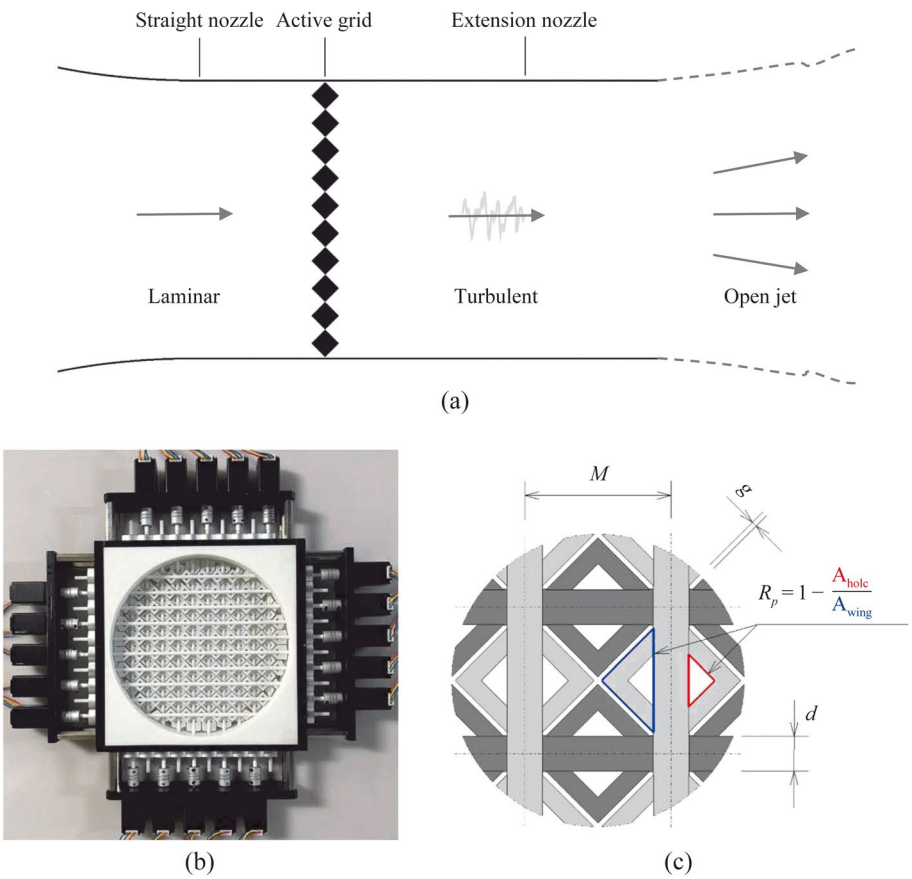

Fig. 5 **a** Schematic of the jet-flow generation section. **b** AG. **c** Schematic of rods and agitator wings in the AG, with $M = 20$ mm, $d = 5$ mm, and $g = 0.7$ mm

errors, are estimated based on the method in Refs. [65–67] and plotted as error bars in some figures for results.

3.1 Baseline laminar flow

The OJF is first assembled into a baseline LJ configuration, which is used to generate high-quality laminar flow for MAV flight experiments at $Re = 10^2 - 10^4$. Here, we utilized the HWA to assess the airspeed stability, uniformity, and the Tu-distribution of LJ. The HWA is an effective technique for capturing unsteady velocities, making it particularly suitable for quantifying turbulence intensity in wind tunnel test sections [68]. In the LJ configuration, the correlation of the fan speed and time-averaged velocity U at $(x/D, y/D, z/D) = (0.1, 0, 0)$ is shown in Fig. 7, along with Tu.

The correlation is in excellent agreement with the linear fit, with a slope of $0.0056 \pm 4.403 \times 10^{-5}$, an intercept of -0.284 ± 0.0278, and the coefficient of determination $R^2 = 0.999$ at 95% confidence.

The OJF can reach a minimum airspeed of 0.1 m/s and a maximum of 16.8 m/s. In general, it shows that $Tu < 0.5\%$ for $U > 1$ m/s and $Tu < 1\%$ for $U \in [0.2, 1]$ m/s. At very low $U < 0.2$ m/s, Tu is slightly higher, around 1% to 3%.

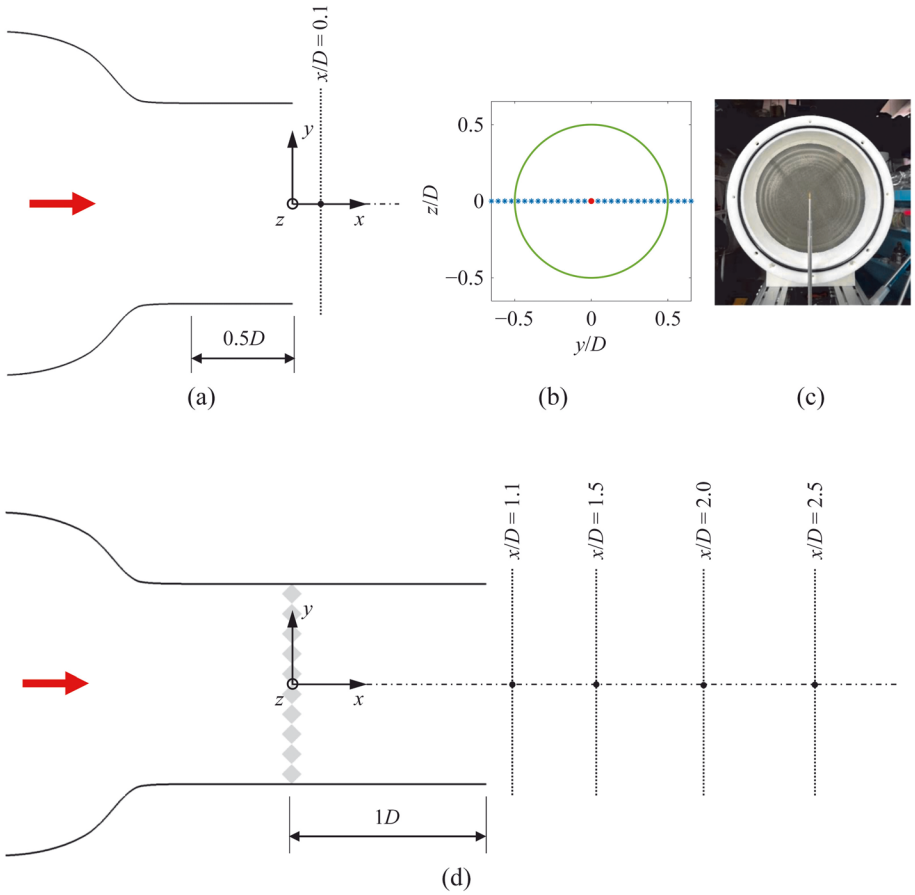

Fig. 6 **a** Measurement planes (dashed lines) in the LJ configuration. **b** Location of measurement points (blue stars) and the diameter of jet exit (green line). **c** Airspeed measurement using the hot film probe. **d** Measurement planes (dashed lines) in the TJ configuration

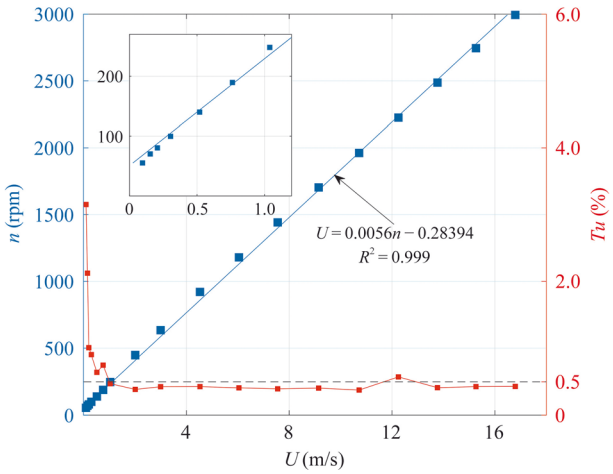

Fig. 7 Left vertical axis: the dependence between the rotational speeds of the fan and the time-averaged axial velocity. Right vertical axis: the relation between the turbulence intensity and the time-averaged axial velocity (*U*)

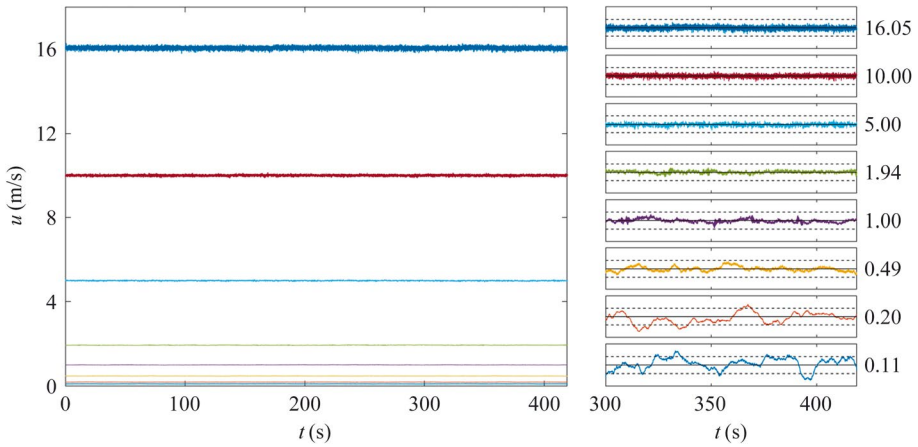

Fig. 8 Left: instantaneous axial velocity at $(x/D, y/D, z/D) = (0.1, 0, 0)$ over the operating airspeed range. Right: closed-up view for comparing the instantaneous axial velocity and the time-averaged one (solid black line with its value shown on the right vertical axis), where the dashed horizontal lines denote $u'/U = \pm 0.02$. For clarity, the data are downsampled by every 100 points when plotting the profiles

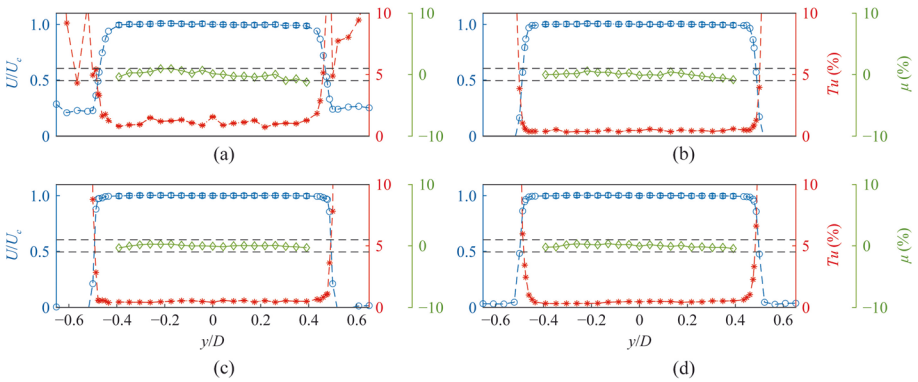

Fig. 9 Normalized time-averaged axial velocity (circles) and turbulence intensity (asterisks) along the radial direction at $x/D = 0.1$for **a** $U_c = 0.21$m/s, **b** $U_c = 1.04$ m/s, **c** $U_c = 4.53$ m/s, and **d** $U_c = 13.77$ m/s. The distribution of measurement points near the shear layer of the jet is refined. The flow uniformity (diamonds) in the cross-sectional region $S = \{(x/D, z/D) = (0.1, 0), y/D \in [-0.4, 0.4]\}$ is plotted, with the reference (dashed) lines for $\mu = \pm 1\%$. Error bars denote measurement uncertainties for velocity and turbulence intensity within the core region with $|\mu| < 1\%$

The flow steadiness over the operating airspeed range is shown in Fig. 8. Airspeeds of eight set points were recorded at $(x/D,\ y/D,\ z/D) = (0.1,\ 0,\ 0)$ within a sampling period of 420 s at 10 kHz. The generated flow is generally steady within a deviation of $u'/U = \pm 0.02$, where u' is the fluctuating axial velocity.

The flow uniformity is assessed from the distribution of U along the radial y-direction (defined in Fig. 6c) at different U_c. Here, U_c denotes the time-averaged axial velocity at $(x/D, y/D, z/D) = (0.1, 0, 0)$. Unless stated otherwise, the hot film acquisition frequency is fixed at 10 kHz for 52 s.

Figure 9 plots U/U_c and Tu at $x/D = 0.1$ for $U_c = 0.21$, 1.04, 4.53, and 13.77 m/s. All of these plots display a flat-topped profile of U. The flow uniformity, with $|\mu| < 1\%$ in the cross-sectional plane $S = \{(x/D, z/D) = (0.1, 0), y/D \in [-0.4, 0.4]\}$ indicates

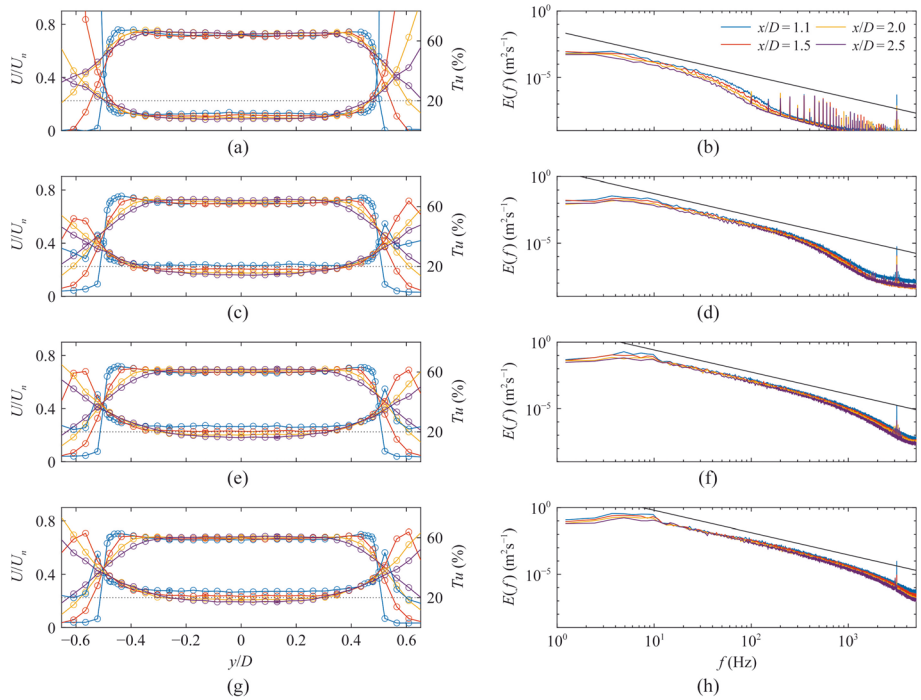

Fig. 10 **a**,**c**,**e**,**g** Normalized time-averaged axial velocity (circles) and turbulence intensity (asterisks) along the radial direction. **b**,**d**,**f**,**h** Temporal power spectral density at the nozzle exit downstream with different x. With the AG ($R_p = 1$), U_n is **a**,**b** 1.04 m/s, **c**,**d** 4.53 m/s, **e**,**f** 9.15 m/s, and **g**,**h** 13.77 m/s. Error bars are added to a few points (within the core region with $|\mu| < 2\%$) to show the typical uncertainty of velocity and turbulence intensity

that the homogeneous core region occupies no less than 80%D. Moreover, Tu remains generally uniform in the core region, with $Tu < 0.5\%$ for $U_c > 1$ m/s and $Tu \approx 1\%$ for $U_c < 1$ m/s, consistent with Fig. 7. The uniformity of the flow field along the z-direction is also excellent (not shown). Considering the axisymmetric design of the OJF, we only used the measurements along the y-direction.

3.2 Turbulent jet flow

The flow quality for a turbulent jet flow is assessed in the TJ configuration of the OJF. A classical Makita-style AG consisting of agitator wings with $R_p = 1$ is added into the LJ configuration, followed by a 1D extension tube to generate a fully developed turbulent flow with a large statistically homogeneous region before the jet diffuses.

The AG was driven in the "double random" mode [69], which can avoid resonance spikes in the energy spectrum at low wavenumbers [46, 70–72]. The grid wings rotate at an angular velocity $\Omega \pm \Delta\Omega = 3.5 \pm 2$ rps (revolution per second), and the duration $T \pm \Delta T = 0.8 \pm 0.7$ s.

The distributions of U and Tu along the y-direction, as well as the temporal power spectral density $E(f)$ in terms of the frequency f are shown in Fig. 10, where $E(f)$ is measured at the center of the measurement plane over a time period of 52 s. The dimensionless velocity profile of U/U_n was measured on four y–z measurement planes at $x/D = 1.1$, 1.5, 2, and 2.5 after the AG along the y-direction, where U_n denotes the

time-averaged axial velocity measured at $(x/D, y/D, z/D) = (0.1, 0, 0)$ without the AG installed. Note that in the TJ configuration the extension tube length is included in the x coordinate, e.g., $x/D = 1.1$ represents the sum of $1D$ for the extension tube and $0.1D$ for the streamwise distance from the measurement point in the free jet.

With the AG installed, the actual jet velocity U is lower than U_n due to the blockage of AG. In Fig. 10, the dimensionless velocity profile of U/U_n along the y-direction exhibits a flat-topped shape. The core region at the downstream AG is generally homogeneous. The flow uniformity μ over $S = \{(x/D, z/D) = (0.1, 0), y/D \in [-0.35, 0.35]\}$ remains $|\mu| < 2\%$. This indicates that the homogeneous core region occupies about $70\%D$. As a result of the jet spreading, the homogeneous zone of the jet diminishes downstream, and the spreading rate grows with decreasing U [73]. There are slight bumps on the outer side of the jet near the exit, perhaps due to the small gap between the AG and the extension tube.

In Fig. 10, Tu grows with U_n, up to about 24% at $U_n = 13.77$ m/s in $x/D = 1.1$, and peaks on the outer sides of the jet. Along the axial direction from $x/D = 1.1$ to $x/D = 2.5$, U remains nearly unchanged, while T_u decreases. The width of the central homogeneous zone of Tu grows with U_n and decays with x. The energy spectrum in the inertial range shows the -5/3 power law and broadens with U_n [70, 74], indicating that the generated turbulent flow is fully developed. The core region with $|\mu| < 2\%$ exhibits similar well-developed energy spectra. Note that no special processing was applied to mitigate industrial frequency interference in the measurements, so the presence of 50 Hz power frequency interference and its harmonics as high frequency peaks were observed in $E(f)$ in Fig. 10, especially at low U_n.

We demonstrate that the present modular OJF operated in the TJ configuration is capable of generating a fully developed turbulent flow in the test area and meanwhile maintaining a wide homogeneous region of $0.7D$. This design meets the demanding requirements of achieving a large, homogeneous, fully developed turbulent field in the OJF test section.

3.3 Controllable turbulence intensity and integral length scale

Generating a turbulent field with controllable turbulence intensity and integral length scale is of importance in designing the wind tunnel and AG. The integral length scale L in the atmospheric boundary layer spans a wide range from centimeters to tens of meters, which has an impact on the flying speed, steadiness, and maneuverability of insects/MAVs [75]. We demonstrate that an improved AG consisting of wings with triangular holes (see Fig. 5c) is able to generate a turbulent flow with controllable Tu and L, where the porosity of AG wings is adjusted by varying the hole area.

The effect of R_p of the AG on the distribution of U/U_n, Tu, and L at $(x, y) = (1.5D, 0)$ along z is shown in Fig. 11. Here, the longitudinal integral length scale L is computed based on the integration of the auto-covariance of u [76] with the method in [77]. In Fig. 11a, c, e, g, U/U_n decays while T_u grows with increasing R_p, indicating the important role of R_p in tuning Tu. Additionally, U/U_n decreases with increasing U_n, i.e., a higher flow velocity results in a greater relative deficit with the same R_p. The overall uniformity of the velocity profile is maintained in the homogeneous region with $W_T/D \approx 0.7$.

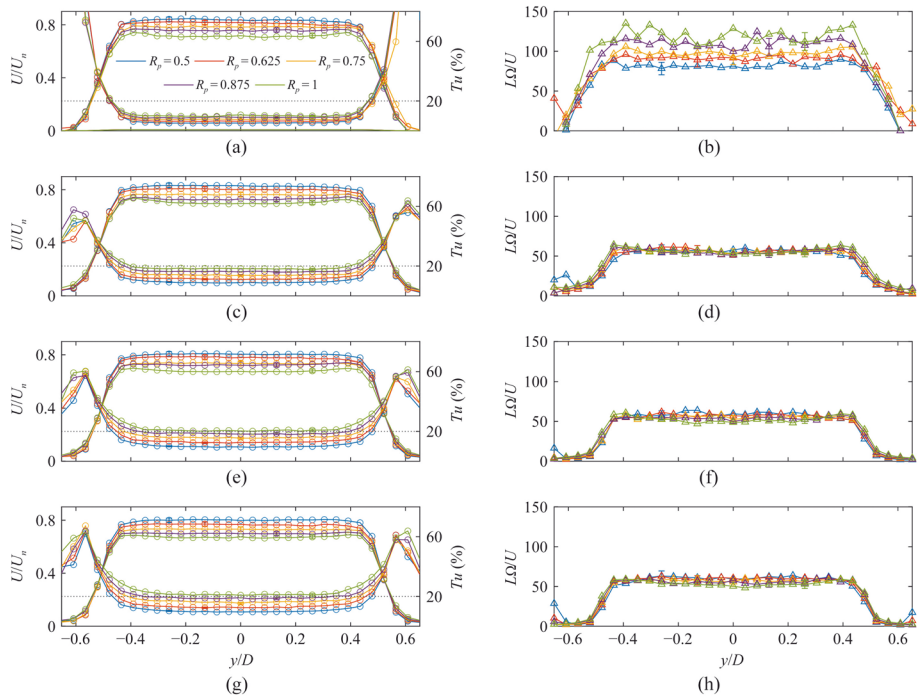

Fig. 11 Distribution of **a**, **c**, **e**, **g** U/U_n and Tu and **b**, **d**, **f**, **g** normalized integral length scale along the y direction at $(x/D, z/D) = (1.5, 0)$ with different R_p at U_n of **a**, **b** 1.04 m/s, **c**, **d** 4.53 m/s, **e**, **f** 9.15 m/s, and **g**, **h** 13.77 m/s. Error bars are added to a few points (within the core region with $|\mu| < 2\%$) to show the typical uncertainty of velocity, turbulence intensity, and integral length scale

Figure 11b, d, f, h plots the distribution of the normalized integral length scale $L\Omega/U$ along z at different x. The flat-topped profile of $L\Omega/U$, similar to the velocity distribution, has a homogeneous region with the width $0.8D$. The collapse of $L\Omega/U$ along z with different R_p demonstrates their self-similarity, except at low speed $U_n = 1.04$ m/s, because the blockage change caused by the AG movement and the disturbance caused by wing rotation can influence the AG-generated turbulence.

The effect of R_p on the turbulence statistics at $(x/D, y/D, z/D) = (1.5, 0, 0)$ or $x/M = 17.25$ at the AG downstream is shown in Table 1. The statistics, including the Kolmogorov length scale $\eta = (\nu^3/\epsilon)^{1/4}$, the Taylor microscale $\lambda = \sigma_u\sqrt{15\nu/\epsilon}$, the Taylor microscale Reynolds number $Re_\lambda = \sigma_u\lambda/\nu$, the mean dissipation rate of turbulent kinetic energy $\epsilon = 15\nu\left\langle\left(\partial u'/\partial t\right)^2\right\rangle/U^2$, are estimated under the assumptions of statistically local homogeneity and isotropy, along with the Taylor frozen hypothesis. Here, $\langle\cdot\rangle$ denotes the time average over 52 s.

The results indicate that the normalized turbulence statistics, including Tu, L, η, Re_λ, and ϵ, can be adjusted by varying R_p at fixed U_n. Namely, the generated turbulence of the OJF is controllable. In general, for fixed AG motion parameters $\Omega \pm \Delta\Omega$ and $T \pm \Delta T$, Tu grows with U_n and R_p. The value of Tu for $R_p = 1$ is almost doubled from that for $R_p = 0.5$; L/M increases with U_n and decreases with R_p at high velocities 4.53, 9.15, and 13.77 m/s; Re_λ increases nonlinearly with R_p and U_n, reaching a maximum near 1500 at 13.77 m/s; η/M decreases with increasing R_p at 4.53, 9.15, and 13.77 m/s; $\epsilon M/U^3$ decreases with U_n and increases with R_p, which shows the

Table 1 Effect of R_p on turbulence statistics measured at $(x/D, y/D, z/D) = (1.5, 0, 0)$

U_n (m/s)	R_p	U/U_n	Tu (%)	Re_λ	L/M	η/M	$\epsilon M/U^3$
1.04	0.5	0.84	5.40	12.1	1.06	0.0277	1.025
1.04	0.625	0.82	6.44	16.4	1.11	0.0279	1.102
1.04	0.75	0.78	7.65	19.6	1.08	0.0267	1.477
1.04	0.875	0.76	9.00	24.5	1.12	0.0262	1.743
1.04	1	0.72	10.69	30.3	1.37	0.0259	2.155
4.53	0.5	0.83	8.86	190.2	3.10	0.0156	0.130
4.53	0.625	0.80	10.97	240.0	2.68	0.0146	0.185
4.53	0.75	0.76	13.80	282.9	2.65	0.0133	0.317
4.53	0.875	0.73	16.04	300.0	2.42	0.0123	0.494
4.53	1	0.70	18.35	311.9	2.40	0.0115	0.746
9.15	0.5	0.80	9.58	453.2	6.28	0.0113	0.061
9.15	0.625	0.78	12.57	635.3	5.80	0.0106	0.089
9.15	0.75	0.74	15.52	733.8	5.05	0.0097	0.147
9.15	0.875	0.71	18.19	744.4	4.93	0.0087	0.261
9.15	1	0.68	20.30	811.2	4.32	0.0085	0.324
13.77	0.5	0.80	9.57	740.8	9.31	0.0097	0.034
13.77	0.625	0.77	12.44	1013.6	9.13	0.0091	0.050
13.77	0.75	0.73	15.38	1187.1	8.02	0.0084	0.081
13.77	0.875	0.70	18.87	1399.6	7.33	0.0077	0.126
13.77	1	0.67	20.81	1443.9	6.67	0.0074	0.169

capability of controlling scale separation in turbulence by adjusting both U_n and R_p. Note that the present AG size is generally smaller than those reported in the literature [44]. The minimum value of R_p here is 0.5, due to challenges in manufacturing grid wings with small R_p. Decreasing R_p could further reduce Tu.

Figure 12 plots the relation between R_p and Tu at $x/D = 1.5$ and $x/D = 2$ for different U_n. In general, Tu increases linearly with R_p, and the increment of Tu diminishes along the flow direction. Moreover, Tu increases with U_n.

The above results demonstrate that the TJ configuration is able to achieve controllable turbulent flow within the test area. The flow with a good uniformity $|\mu| < 2\%$ in the core region occupies about 70%D. It is possible to achieve continuously adjustable turbulence in real time by further optimizing the control strategy of R_p.

4 Conclusions

We design the OJF operating at very low speed and high turbulence intensity for bio-inspired MAV/insect flight experiments. The OJF can be also used for anemometer calibration, e.g., hot wire/film probes, vane anemometers, and multi-hole pressure probes in low-speed and highly unsteady wind environments.

The key techniques/concepts in designing the OJF are summarized below. First, a stage-driven motor is designed to power the fan of the OJF, enabling it to generate wind speeds covering a typical range of airspeeds for MAV flight experiments. The minimum speed is as low as 0.1 m/s, and the speed ratio is up to 100:1.

Second, the optimized flow conditioning section integrates a variable-density screen to pre-rectify the wake deficit of the axial fan wake flow, along with a 3:1 contraction

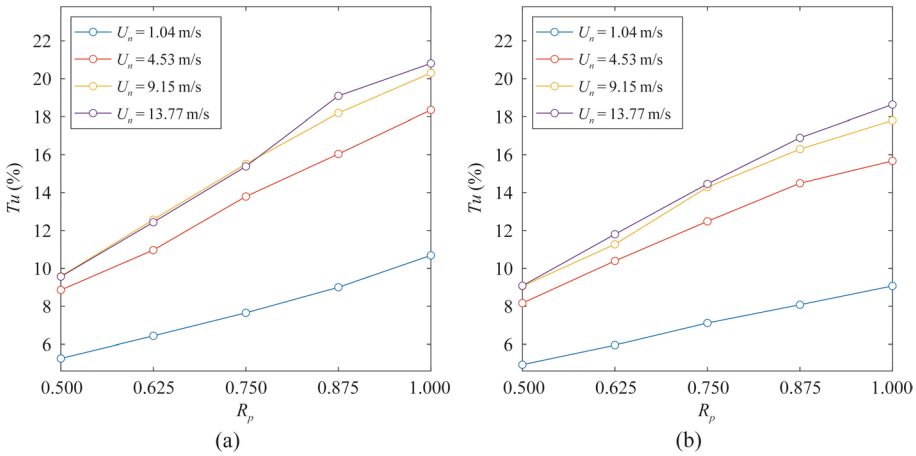

Fig. 12 The relation between R_p and Tu under different U_n at **a** $x/D = 1.5$ and **b** $x/D = 2$

optimized through an adjoint-driven method based on the inlet velocity. This configuration enables the OJF to generate high-quality flows across a large test section area, which is up to two to three times larger than conventional designs with a contraction ratio ranging from 6:1 to 10:1.

Third, the modularized design of the jet generation nozzles has two configurations. The baseline LJ configuration produces high-quality laminar flow. The TJ configuration, featured by an AG consisting of improved wings with triangular holes, can generate controllable turbulent wind conditions.

Flow field calibration results show that the OJF in the LJ configuration can generate a high-quality baseline flow with a steady wind speed of $0.1 - 16.8$ m/s and low turbulence intensity $Tu \approx 0.5\%$ in a uniform region covering above 80%D. In the TJ configuration, the OJF can generate a fully developed turbulent jet flow with Tu up to 24% in a statistically homogeneous region close to 70%D.

In the future work, the OJF can reproduce wind shear and gusts in MAV flight experiments, and elucidate flow mechanisms of AG-generated turbulence. Multiple OJFs can form a large array with a larger cross-sectional area such as 3×3 m^2 for MAV swarm applications.

Appendix A: Aerodynamic load of the NACA0012 airfoil at low speed and high turbulence intensity

In-flight disturbances, such as turbulence, induce additional loads that can impact the aerodynamic efficiency and stability of MAVs. To demonstrate the capability of the present OJF at low speed and high turbulence intensity, we illustrate the influence of turbulence intensity on the aerodynamic load of the NACA0012 airfoil at low Re.

The airfoil with chord length $C = 0.06$ m and span $B = 0.1188$ m has an aspect ratio close to 2. It is manufactured using photosensitive resin and 3D printing, and its surface is polished to achieve a smooth finish. The inlet velocity is 10.2 m/s, corresponding to $Re \approx 3.9 \times 10^4$. Four typical flow conditions, $Tu = 0.5\%$ (no AG), $Tu = 2.4\%$ (AG in passive mode with agitator wings aligned with the mean flow), $Tu = 8.9\%$, and

$Tu = 19.5\%$ (AG with wings of $R_p = 0.5$ and 1, respectively, with $\Omega \pm \omega = 3.5 \pm 2$ rps, $T \pm \Delta T = 0.8 \pm 0.7$ s), are adopted. These turbulence intensities were measured at $x/D = 0.5$ from the OJF outlet. Then the airfoil was installed, and the airfoil 1/4 aerodynamic center is also located at $x/D = 0.5$.

As sketched in Fig. 13a, the airfoil is linked to a three-component force balance (LMC3501A-10N, Nissho) via a steel rod at its 1/4 aerodynamic center. Thus, the lift F_L and drag F_D can be measured at the frequency 5 kHz. Here, we denote time-averaged lift as F_L, time-averaged drag as F_D, and instantaneous lift and drag as F_l and F_d, respectively, and their corresponding coefficients as $C_L = 2F_L/(\rho U^2 CB)$, $C_D = 2F_D/(\rho U^2 CB)$, $C_l = 2F_l/(\rho U^2 CB)$, and $C_d = 2F_d/(\rho U^2 CB)$. The force balance connecting to a turntable enables aerodynamic measurements from $-5°$ to $25°$ with the interval of $1°$ and accuracy of $0.025°$. To maintain two-dimensionality, endplates on both sides of the airfoil are positioned approximately 1 mm from the model tip and securely affixed to the OJF outlet. Corrections [78] were applied to the aerodynamic forces and angle of attack α. The uncertainty for C_L and C_D is estimated using the method outlined in Ref. [79] and plotted in Fig. 13 as error bars.

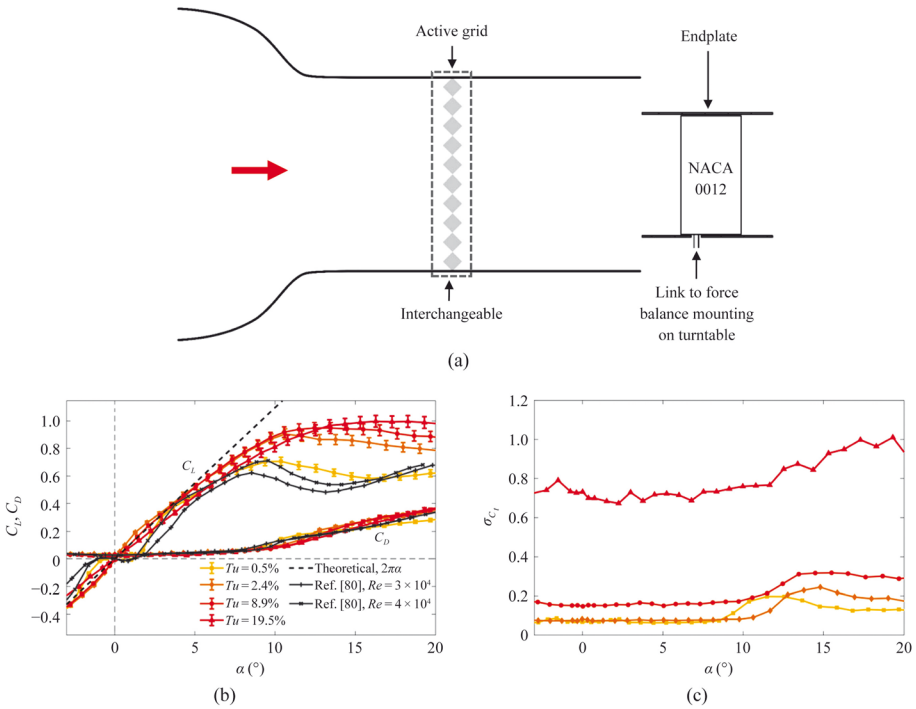

Fig. 13 **a** Schematic for the OJF and the measurement of the aerodynamic load of the NACA0012 airfoil. **b** Lift and drag coefficients versus the angle of attack at $Re \approx 3.9 \times 10^4$ and various turbulence intensities, along with the theoretical result and the experimental results in Ref. [80]. **c** Fluctuations of the total aerodynamic force coefficient versus the angle of attack at $Re \approx 3.9 \times 10^4$ and various turbulence intensities

Figure 13b plots the profile of $C_L = 2F_L/(\rho U^2 CB)$ versus α with various Tu. At $Tu = 0.5\%$, the profile of C_L shows a dip around $0°$. Then, up to $\alpha \approx 4°$, C_L grows steeper than the theoretical estimation $2\pi\alpha$. Finally, the growth slows down, reaching stall near $\alpha = 10°$. This result generally agrees with that in Ref. [80] for

$Re = 3 \times 10^4 - 4 \times 10^4$ at $Tu = 0.1\%$, except for slight discrepancies perhaps due to inflow turbulence and blockage corrections.

The turbulence intensity has an impact on C_L. As Tu increases, the negative lift near 0° disappears. For $\alpha = 3° - 10°$, the overall growth of C_L (versus α) is enhanced with Tu from 0.5% to 8.9%, whereas it is mitigated with $Tu = 19.5\%$. The stall angle and the maximum C_L grow with Tu. In addition, $C_D = 2F_D/(\rho U^2 CB)$ at different Tu are similar before stall for small α, whereas C_D increases with Tu for $\alpha > 10°$ due to post-stall changes in pressure drag.

Figure 13c plots the standard deviation σ_{C_t} of the coefficient $C_t = 2\sqrt{F_l^2 + F_d^2}/(\rho U^2 CB)$ of the total force. The overall load fluctuation increases with Tu, e.g., σ_{C_t} at $Tu = 19.5\%$ is about eight times of that at $Tu = 0.5\%$. Moreover, σ_{C_t} has minor variations before stall and rises after stall, and the largest growth of σ_{C_t} occurs at $Tu = 19.5\%$.

These observations indicate that Tu has an impact on airfoil fatigue loads. Therefore, the present OJF operating at a range of Tu can facilitate understanding the influence of Tu on airfoil loads and developing control methods for MAVs in atmospheric turbulence.

Acknowledgements
Not applicable.

Authors' contributions
ZL and YY designed the project and ZL conducted the research. ZL and YY analyzed the experimental result and wrote the manuscript. All authors read and approved the final manuscript.

Funding
This work has been supported in part by the National Natural Science Foundation of China (Grant Nos. 11925201 and 11988102), the National Key R&D Program of China (Grant No. 2020YFE0204200), and the Xplorer Prize.

Availability of data and materials
All data and materials are available upon reasonable request.

Declarations

Competing interests
The authors report no conflicts of interest.

Received: 14 January 2024 Accepted: 5 May 2024
Published online: 02 August 2024

References

1. Shyy W, Aono H, Kang CK et al (2013) An introduction to flapping wing aerodynamics. Cambridge University Press, Cambridge
2. Moriche M, Flores O, García-Villalba M (2017) On the aerodynamic forces on heaving and pitching airfoils at low reynolds number. J Fluid Mech 828:395–423
3. Corkery SJ, Babinsky H, Harvey JK (2018) On the development and early observations from a towing tank-based transverse wing-gust encounter test rig. Exp Fluids 59(9):135
4. Combes SA, Dudley R (2009) Turbulence-driven instabilities limit insect flight performance. Proc Natl Acad Sci U S A 106(22):9105–9108
5. Crall JD, Chang JJ, Oppenheimer RL et al (2017) Foraging in an unsteady world: bumblebee flight performance in field-realistic turbulence. Interface Focus 7(1):20160086
6. Engels T, Kolomenskiy D, Schneider K et al (2019) Impact of turbulence on flying insects in tethered and free flight: High-resolution numerical experiments. Phys Rev Fluids 4:013103
7. Andreu-Angulo I, Babinsky H, Biler H et al (2020) Effect of transverse gust velocity profiles. AIAA J 58(12):5123–5133
8. Bomphrey RJ, Godoy-Diana R (2018) Insect and insect-inspired aerodynamics: unsteadiness, structural mechanics and flight control. Curr Opin Insect Sci 30:26–32
9. Olejnik DA, Muijres FT, Karásek M et al (2022) Flying into the wind: Insects and bio-inspired micro-air-vehicles with a wing-stroke dihedral steer passively into wind-gusts. Front Robot AI 9:820363
10. Lighthill MJ (1973) On the Weis-Fogh mechanism of lift generation. J Fluid Mech 60(1):1–17
11. Ellington CP, van den Berg C, Willmott AP et al (1996) Leading-edge vortices in insect flight. Nature 384(6610):626–630

12. Dickinson MH, Lehmann FO, Sane SP (1999) Wing rotation and the aerodynamic basis of insect flight. Science 284(5422):1954–1960
13. Sun M, Tang J (2002) Unsteady aerodynamic force generation by a model fruit fly wing in flapping motion. J Exp Biol 205(1):55–70
14. Bomphrey RJ, Nakata T, Phillips N et al (2017) Smart wing rotation and trailing-edge vortices enable high frequency mosquito flight. Nature 544(7648):92–95
15. Zhu HJ, Sun M (2017) Unsteady aerodynamic force mechanisms of a hoverfly hovering with a short stroke-amplitude. Phys Fluids 29(8):081901
16. Zhang JD, Huang WX (2019) On the role of vortical structures in aerodynamic performance of a hovering mosquito. Phys Fluids 31(5):051906
17. Liu LG, Du G, Sun M (2020) Aerodynamic-force production mechanisms in hovering mosquitoes. J Fluid Mech 898:A19
18. Tong W, Yang Y, Wang S (2021) Estimating thrust from shedding vortex surfaces in the wake of a flapping plate. J Fluid Mech 920:A10
19. Tong W, Wang S, Yang Y (2022) Estimating forces from cross-sectional data in the wake of flows past a plate using theoretical and data-driven models. Phys Fluids 34(11):111905
20. Barlow JB, Pope A, Rae W (1999) Low-speed wind tunnel testing, 3rd edn. Wiley, New York
21. Barelle C (2011) Sport aerodynamics: On the relevance of aerodynamic force modelling versus wind tunnel testing. In: Lerner JC, Boldes U (ed) Wind tunnels and experimental fluid dynamics research. IntechOpen, London
22. Kaufmann C, Briegel H (2004) Flight performance of the malaria vectors Anopheles gambiae and Anopheles atroparvus. J Vector Ecol 29(1):140–153
23. Wenner AM (1963) The flight speed of honeybees: a quantitative approach. J Apic Res 2(1):25–32
24. Whitehouse FC, Walker EM (1941) British Columbia dragonflies (Odonata), with notes on distribution and habits. Am Midl Nat 26(3):488–557
25. Tennekes H (2009) The simple science of flight: from insects to jumbo jets, revised and expanded edition. The MIT Press, Cambridge
26. Plate EJ, Cermak JE (1963) Micrometeorological wind tunnel facility: description and characteristics. Cont Rep CER63EJP-JEC9, Colorado State University, Fort Collins
27. Terao Y, Takamoto M, Katagiri T (1997) Very low speed wind tunnel for anemometer calibration. Trans Japan Soc Mech Eng B 63(607):938–943
28. Sun YT, Zhu XY (2006) Characteristics of ultra-low speed wind tunnels for research on micro-UAV. J Exp Fluid Mech 20(1):58–61
29. Leith JR, Raether AM, Smith DK (1988) Wind tunnel facility for operation at very low velocity. J Phys E Sci Instrum 21(5):497–501
30. Pezzotti S, D'Iorio JI, Nadal-Mora V et al (2011) A wind tunnel for anemometer calibration in the range of 0.2–1.25 m/s. Flow Meas Instrum 22(4):338–342
31. Batchelor GK (1953) The theory of homogeneous turbulence. Cambridge University Press, Cambridge
32. Roach PE (1987) The generation of nearly isotropic turbulence by means of grids. Int J Heat Fluid Flow 8(2):82–92
33. Gomes-Fernandes R, Ganapathisubramani B, Vassilicos JC (2012) Particle image velocimetry study of fractal-generated turbulence. J Fluid Mech 711:306–336
34. Zhao Y, Yang Y, Li M et al (2023) Measurements of decaying grid turbulence with various initial conditions. Eur J Mech B Fluids 102:46–55
35. Gad-El-Hak M, Corrsin S (1974) Measurements of the nearly isotropic turbulence behind a uniform jet grid. J Fluid Mech 62(1):115–143
36. Masuk AUM, Salibindla A, Tan S et al (2019) V-ONSET (Vertical Octagonal Noncorrosive Stirred Energetic Turbulence): A vertical water tunnel with a large energy dissipation rate to study bubble/droplet deformation and breakup in strong turbulence. Rev Sci Instrum 90(8):085105
37. Makita H, Sassa K (1991) Active turbulence generation in a laboratory wind tunnel. In: Johansson AV, Alfredsson PH (eds) Advances in turbulence 3. Springer, Berlin, Heidelberg, pp 497–505
38. Ozono S, Ikeda H (2018) Realization of both high-intensity and large-scale turbulence using a multi-fan wind tunnel. Exp Fluids 59(12):187
39. Wang JY, Zeng M, Meng QH (2019) Latticed mode: A new control strategy for wind field simulation in a multiple-fan wind tunnel. Rev Sci Instrum 90(8):085104
40. Li X, Yao Y, Zhao B et al (2019) Characteristics and performances of a small-scale model of the closed-circuit multiple controlled fan wind tunnel. Rev Sci Instrum 90(4):045104
41. Yang B, Zhang B, Zhou X et al (2020) Artificial simulation of complex unsteady wind in an ABL wind tunnel with dual axial fans. J Wind Eng Ind Aerodyn 197:104075
42. Olejnik DA, Wang S, Dupeyroux J et al (2022) An experimental study of wind resistance and power consumption in MAVs with a low-speed multi-fan wind system. In: 2022 international conference on robotics and automation (ICRA), Philadelphia, 12 July 2022
43. Walpen A, Catry G, Noca F (2023) Real-scale atmospheric wind and turbulence replication using a fan-array for environmental testing and UAV/AAM validation. In: AIAA SCITECH 2023 forum, National Harbor, 23-27 January 2023
44. Mydlarski L (2017) A turbulent quarter century of active grids: from Makita (1991) to the present. Fluid Dyn Res 49(6):061401
45. Cekli HE, van de Water W (2010) Tailoring turbulence with an active grid. Exp Fluids 49(2):409–416
46. Larssen JV, Devenport WJ (2011) On the generation of large-scale homogeneous turbulence. Exp Fluids 50(5):1207–1223
47. Bodenschatz E, Bewley GP, Nobach H et al (2014) Variable density turbulence tunnel facility. Rev Sci Instrum 85(9):093908
48. Hearst RJ, Ganapathisubramani B (2017) Tailoring incoming shear and turbulence profiles for lab-scale wind turbines. Wind Energy 20(12):2021–2035

49. Neuhaus L, Hölling M, Bos WJT et al (2020) Generation of atmospheric turbulence with unprecedentedly large Reynolds number in a wind tunnel. Phys Rev Lett 125(15):154503
50. Sytsma MJ (2013) Effects of turbulence on fixed wing small unmanned aerial systems. Dissertation, University of Florida
51. Hart A, Sytsma M, Ukeiley L (2016) An aerodynamic characterization facility for micro air vehicle research. Int J Micro Air Veh 8(2):79–91
52. Quinn DB, Watts A, Nagle T et al (2017) A new low-turbulence wind tunnel for animal and small vehicle flight experiments. R Soc Open Sci 4(3):160960
53. Wallis RA (2014) Axial flow fans: design and practice. Academic Press, New York
54. Guan XF (2011) Modern pumps theory and design. China Astronautic Publishing, Beijing
55. Su YX (1991) Flow analysis and design of three-dimensional wind tunnel contractions. AIAA J 29(11):1912–1920
56. Breuer K, Drela M, Fan X et al (2022) Design and performance of an ultra-compact, low-speed, low turbulence level, wind tunnel for aerodynamic and animal flight experiments. Exp Fluids 63(11):169
57. Kao YH, Jiang ZW, Fang SC (2017) A computational simulation study of fluid mechanics of low-speed wind tunnel contractions. Fluids 2(2):23
58. Leifsson L, Koziel S (2015) Simulation-driven design of low-speed wind tunnel contraction. J Comput Sci 7:1–12
59. Jameson A (2003) Aerodynamic shape optimization using the adjoint method. Lectures at the Von Karman Institute, Brussels, 6 February 2003
60. Xu M, Wei M (2016) Using adjoint-based optimization to study kinematics and deformation of flapping wings. J Fluid Mech 799:56–99
61. Pope SB (2000) Turbulent flows. Cambridge University Press, Cambridge
62. Bell JH, Mehta RD (1988) Contraction design for small low-speed wind tunnels. NASA Cont Rep NASA-CR-182747
63. Menter FR (1994) Two-equation eddy-viscosity turbulence models for engineering applications. AIAA J 32(8):1598–1605
64. Mehta R, Bradshaw P (1979) Design rules for small low speed wind tunnels. Aeronaut J 83(827):443–453
65. Abernethy RB, Benedict RP, Dowdell RB (1985) ASME measurement uncertainty. ASME J Fluids Eng 107(2):161–164
66. Jørgensen FE (2001) How to measure turbulence with hot-wire anemometers: a practical guide. Dantec Dynamics, Skovlunde
67. Benedict LH, Gould RD (1996) Towards better uncertainty estimates for turbulence statistics. Exp Fluids 22(2):129–136
68. Bruun HH (1996) Hot-wire anemometry: principles and signal analysis. Meas Sci Technol 7(10):024
69. Poorte R, Biesheuvel A (2002) Experiments on the motion of gas bubbles in turbulence generated by an active grid. J Fluid Mech 461:127–154
70. Mora DO, Muñiz Pladellorens E, Riera Turró P et al (2019) Energy cascades in active-grid-generated turbulent flows. Phys Rev Fluids 4:104601
71. Shet CS, Cholemari MR, Veeravalli SV (2020) Optimizing the performance of an active grid to generate high intensity isotropic free stream turbulence. Phys Fluids 32(9):095120
72. Zheng Y, Nagata K, Watanabe T (2021) Turbulent characteristics and energy transfer in the far field of active-grid turbulence. Phys Fluids 33(11):115119
73. Pollard A (2020) Turbulent round jet entrainment–A historical perspective. In: Runchal A (ed) 50 years of CFD in engineering sciences. Springer, Singapore, pp 269–294
74. Puga AJ, LaRue JC (2017) Normalized dissipation rate in a moderate Taylor Reynolds number flow. J Fluid Mech 818:184–204
75. Watkins S, Mohamed A, Fisher A et al (2015) Towards autonomous MAV soaring in cities: CFD simulation, EFD measurement and flight trials. Int J Micro Air Veh 7(4):441–448
76. Lenschow DH, Stankov BB (1986) Length scales in the convective boundary layer. J Atmos Sci 43(12):1198–1209
77. Cheynet E (2016) Wind-induced vibrations of a suspension bridge: A case study in full-scale. Dissertation, University of Stavanger
78. Garner HC, Rogers E, Acum W et al (1966) Subsonic wind tunnel wall corrections. AGARD, Paris
79. Stutz C, Hrynuk J, Bohl D (2022) Investigation of static wings interacting with vertical gusts of indefinite length at low Reynolds numbers. Exp Fluids 63(5):82
80. Ohtake T, Nakae Y, Motohashi T (2007) Nonlinearity of the aerodynamic characteristics of NACA0012 aerofoil at low Reynolds numbers. J Japan Soc Aeronaut Space Sci 55(644):439–445

Publisher's Note